Anti-PT-Symmetric Optical Gyroscope at the Transmission Peak Degeneracy With Enhanced Signal-to-Noise Ratio

Martino De Carlo ⬤, Francesco De Leonardis ⬤, *Senior Member, IEEE,* and Vittorio M. N. Passaro ⬤, *Senior Member, IEEE*

Abstract—Non-Hermitian sensors have been widely studied for the enhanced response of their eigenvalues in the proximity of exceptional points. However, it has been shown that noise is enhanced in the same way as sensitivity, thus vanishing the advantages of the exceptional point. Recently, the idea of measuring the frequency splitting of transmission peaks of a non-lasing PT-symmetric sensor has shown the possibility of increasing the signal-to-noise ratio of a sensor close to the so called "transmission peak degeneracy", with respect to an operating condition away from it. Here we analyze a non-Hermitian optical gyroscope, demonstrating that also anti-PT-symmetric Hamiltonians show an enhanced transmission peaks frequency splitting in the proximity of the transmission peak degeneracy. We also perform an analysis on noise and uncertainties and introduce new figures of merit to compare the proposed anti-PT-symmetric sensor with a classical resonant optical gyroscope. When the uncertainties due to fluctuations of parameters are negligible with respect to the uncertainties due to amplitude noise, the non-Hermitian sensor working at the transmission peak degeneracy is demonstrated to operate better than a classical resonant gyroscope in terms of signal-to-noise ratio.

Index Terms—Exceptional points, gyroscopes, noise, non-Hermitian, PT-symmetry, resonators, signal-to-noise ratio, transmission peak degeneracy.

I. INTRODUCTION

THE widespread interest in exceptional points (EPs) of non-Hermitian (NH) Hamiltonians, especially for sensing applications [1], [2], takes its origin from the pioneering research by Bender et al. [3]. In particular, it was demonstrated that a particular form of non-Hermitian Hamiltonians commuting with the joint operations of parity (*P*) and time (*T*) operators shows real eigenvalues. One of the interesting properties of these systems is the presence of an exceptional point, representing the

degeneracy where the eigenvalues and the corresponding eigenstates coalesce simultaneously. The strong spectral response of the eigenvalues in the proximity of EPs inspired a lot of research works for sensing applications, especially with photonic [4], [5], [6], [7], [8], [9], [10], [11], [12], [13] and electronic approaches [14], [15], [16]. Specifically in photonics, NH Hamiltonians have been mainly applied to angular velocity sensing [17], [18], [19], [20], [21], [22] and particle sensing [23], [24], [25], [26], [27].

In 2×2 NH Hamiltonians working at the EP, the eigenvalue splitting depends on the square root of the applied perturbation, thus showing an enhanced sensitivity for small values of perturbations. However, recently it has been shown that the simultaneous divergence of the noise and of the sensitivity of the eigenfrequency splitting at the EP cancels the advantage of non-Hermitian sensing [28], [29], [30], [31].

To overcome this problem, a non-lasing PT-symmetric electronic accelerometer coupled to a transmission line has been realized [32]. Using the frequency splitting of the transmission peaks as the output of the sensor, rather than eigenfrequency splitting, has been shown to enhance the signal-to-noise ratio. In particular, the transmission peak frequencies collapse at a design condition called "transmission peak degeneracy" (TPD), where the sensitivity diverges. In this way the authors were able to separate the condition of the divergence of the sensitivity (corresponding to the TPD) from the condition of divergence of the noise (corresponding to the EP). In this work we apply the concept of the TPD to anti-PT-symmetric Hamiltonian for angular velocity sensing. We show that also anti-PT-symmetric systems show a TPD distinct from the EP, thus making it possible to enhance the signal-to-noise ratio. Moreover, we demonstrate that it is possible to set the TPD (and consequently the maximum sensitivity) in condition of null perturbation (zero angular velocity). Then, we propose a new approach for comparing the TPD-based sensor to a classical configuration of the same sensor. In our analysis, we demonstrate that for certain operating conditions a non-Hermitian gyroscope shows better performance than a classical resonant gyroscope in terms of signal-to-noise ratio.

II. MODELLING

A. Non-Hermitian Hamiltonian

In [32] it has been experimentally demonstrated that working next to a TPD of a non-Hermitian Hamiltonian can increase the
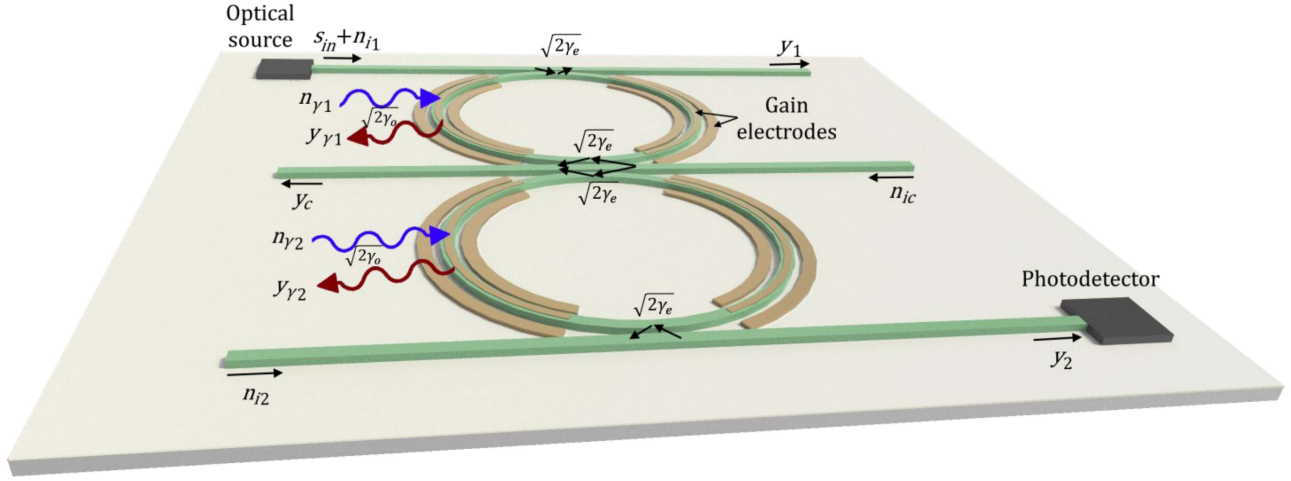
Fig. 1. Rendering of the non-Hermitian optical gyroscope with labels indicating the input and output signals.

signal-to-noise ratio of a sensor. In particular, a quasi-parity-time symmetric effective Hamiltonian has been set up, in order to obtain a transmission peak degeneracy distinct from the exceptional point (EP). Here we want to demonstrate the feasibility of an anti-PT-symmetric gyroscope with the architecture proposed in Fig. 1. In order to simultaneously consider the signal and noise inputs, the device is modelled as an open system with two optical resonators and five total ports (three physical buses and two phantom buses connecting the resonators with the gain/loss reservoirs). The amplitude vector:

$$\boldsymbol{a} = \begin{pmatrix} a_1 \\ a_2 \end{pmatrix} \qquad (1)$$

represents the amplitudes inside the optical cavity, normalized such that $|a_{1(2)}|^2$ corresponds to the energy stored in the first (second) resonators. Using the temporal coupled-mode theory formalism for optical resonators, we can write [22], [32], [33]:

$$\frac{d\boldsymbol{a}}{dt} = j\boldsymbol{H}_0\boldsymbol{a} + \boldsymbol{K}^T\boldsymbol{x} \qquad (2)$$

$$\boldsymbol{y} = \boldsymbol{C}\boldsymbol{x} + \boldsymbol{K}\boldsymbol{a} \qquad (3)$$

with $\boldsymbol{H}_0$ the effective Hamiltonian, $\boldsymbol{K}$ the 5×2 coupling matrix, $\boldsymbol{C}$ a 5×5 scattering matrix, $\boldsymbol{x}$ the exciting incoming waves, $\boldsymbol{y}$ the outgoing waves. In particular, $\boldsymbol{H}_0$, $\boldsymbol{x}$ and $\boldsymbol{y}$ can be written as (in the linear hypothesis, i.e., much below the saturation conditions) [32], [33]:

$$\boldsymbol{H}_0 = \begin{pmatrix} \omega_1 + 2j\gamma_e \pm j\gamma_0 & j\gamma_e \\ j\gamma_e & \omega_2 + 2j\gamma_e \pm j\gamma_0 \end{pmatrix} \qquad (4)$$

$$\boldsymbol{x} = \begin{pmatrix} s_{in} + n_{i1} \\ n_{ic} \\ n_{i2} \\ n_{\gamma 1} \\ n_{\gamma 2} \end{pmatrix}, \boldsymbol{y} = \begin{pmatrix} y_1 \\ y_c \\ y_2 \\ y_{\gamma 1} \\ y_{\gamma 2} \end{pmatrix}. \qquad (5)$$

In particular, $\omega_{1(2)}$ is the isolated resonance of the first (second) resonator, γ_o represents the intrinsic loss rate (with the "+" sign) or intrinsic gain rate (with the "-" sign) of each resonator, whereas γ_e is the loss rate due to the coupling with each of

the two buses adjacent to each resonator. Then, s_{in} is the input amplitude wave (normalized such that $|s_{in}|^2$ represents the input power), and n_{i1}, n_{i2} and n_{ic} are the input noise amplitudes arising from the coupling with external physical buses, whereas $n_{\gamma 1}$ and $n_{\gamma 2}$ are the input amplitudes of the noise arising from the coupling with the gain/loss reservoirs (Fig. 1). Finally, y_1, y_2, y_c are the output amplitudes at the physical buses, and $y_{\gamma 1}$ and $y_{\gamma 2}$ are the output amplitudes at the gain/loss reservoirs.

According to the constraint $\boldsymbol{C}\boldsymbol{K}^* = -\boldsymbol{K}$ [33], we set $\boldsymbol{C}$ and $\boldsymbol{K}$ as [32]:

$$\boldsymbol{C} = \begin{pmatrix} -1 & 0 & 0 & 0 & 0 \\ 0 & -1 & 0 & 0 & 0 \\ 0 & 0 & -1 & 0 & 0 \\ 0 & 0 & 0 & -1 & 0 \\ 0 & 0 & 0 & 0 & -1 \end{pmatrix} \qquad (6)$$

$$\boldsymbol{K} = \begin{pmatrix} \sqrt{2\gamma_e} & 0 \\ \sqrt{2\gamma_e} & \sqrt{2\gamma_e} \\ 0 & \sqrt{2\gamma_e} \\ \sqrt{2\gamma_o} & 0 \\ 0 & \sqrt{2\gamma_o} \end{pmatrix} \qquad (7)$$

with $(2\gamma_e)^{1/2}$ the mutual coupling between each physical bus and each resonator next to it and $(2\gamma_o)^{1/2}$ the mutual coupling between each gain/loss reservoir and the corresponding resonator.

By setting $\gamma_t = 2\gamma_e \pm \gamma_o$, $\kappa_0 = \gamma_e$, $\omega_0 = (\omega_1 + \omega_2)/2$ and $\Delta = (\omega_1 - \omega_2)/2$, we obtain:

$$\boldsymbol{H}_0 = \begin{pmatrix} \omega_0 + \Delta + j\gamma_t & j\kappa_0 \\ j\kappa_0 & \omega_0 - \Delta + j\gamma_t \end{pmatrix}. \qquad (8)$$

In (2) $\boldsymbol{H}_0$ plays the role of an effective Hamiltonian in unperturbed conditions (at rest), and it is anti-parity-time-symmetric $(PT\boldsymbol{H}_0(PT)^{-1} = -\boldsymbol{H}_0)$. To take into account the rotation, we add an opposite perturbation $\epsilon_{1(2)}$ on the resonance frequencies [17] (due to the Sagnac effect). For simplicity we will assume the two resonators to have almost the same area and perimeter, so the perturbation is considered to be the same on the two resonators

$(\epsilon = \epsilon_1 \approx \epsilon_2)$. The perturbed Hamiltonian will be expressed as:

$$\boldsymbol{H} = \begin{pmatrix} \omega_0 + \Delta + j\gamma_t + \epsilon & j\kappa_0 \\ j\kappa_0 & \omega_0 - \Delta + j\gamma_t - \epsilon \end{pmatrix}. \quad (9)$$

In this case, $\boldsymbol{H}$ represents the effective Hamiltonian in the perturbed condition (during rotation).

B. Non-Hermitian Gyroscope

The eigenfrequencies are immediately obtained from the secular equation ($\boldsymbol{H} - \omega_{eig}\boldsymbol{I} = 0$, with $\boldsymbol{I}$ the identity matrix) as:

$$\omega_{\text{eig}} = \omega_0 + j\gamma_t \pm \sqrt{(\epsilon + \Delta)^2 - \kappa_0^2}. \quad (10)$$

An EP arises for

$$\epsilon_{EP} = -\Delta \pm |\kappa_0|. \quad (11)$$

Whereas the lasing threshold is obtained for $\text{Im}\{\omega_{eig}\} = 0$:

$$\epsilon_L = -\Delta \pm \sqrt{\kappa_0^2 - \gamma_t^2} \quad (12)$$

with

$$(\epsilon + \Delta)^2 - \kappa_0^2 < 0. \quad (13)$$

In order to calculate the transfer function of the system when is subject to a rotation, we calculate the Green's Matrix,

$$\boldsymbol{G} = (\boldsymbol{H} - \omega\boldsymbol{I})^{-1} \quad (14)$$

whose elements are:

$$G_{11} = \frac{\omega_0 - \Delta + j\gamma_t - \epsilon - \omega}{(\omega - \omega_0 - j\gamma_t)^2 - (\Delta + \epsilon)^2 + \kappa_0^2} \quad (15a)$$

$$G_{12} = G_{21} = \frac{-j\kappa_0}{(\omega - \omega_0 - j\gamma_t)^2 - (\Delta + \epsilon)^2 + \kappa_0^2} \quad (15b)$$

$$G_{22} = \frac{\omega_0 + \Delta + j\gamma_t + \epsilon - \omega}{(\omega - \omega_0 - j\gamma_t)^2 - (\Delta + \epsilon)^2 + \kappa_0^2}. \quad (15c)$$

The transfer function $T_{12} = |y_2/s_{in}|^2$ is obtained as:

$$\begin{aligned} T_{12} &= |S_{12}|^2 = 4\gamma_e^2 |G_{12}|^2 \\ &= \frac{4\gamma_e^2\kappa_0^2}{\left((-\omega_0 + \omega)^2 - \gamma_t^2 - (\Delta + \epsilon)^2 + \kappa_0^2\right)^2 + 4\gamma_t^2(\omega - \omega_0)^2}. \end{aligned} \quad (16)$$

We can easily calculate the peak frequencies (ω_p), i.e., the angular frequencies for which the transfer function T_{12} has transmission peaks, for:

$$\frac{dT_{12}}{d\omega} = 0. \quad (17)$$

After defining $\xi = (\epsilon + \Delta)^2 - \kappa_0^2 - \gamma_t^2$, we obtain the peak frequencies as:

$$\omega_p = \begin{cases} \omega_0 & \text{for } \xi < 0 \\ \omega_0 \pm \sqrt{(\epsilon + \Delta)^2 - \kappa_0^2 - \gamma_t^2} & \text{for } \xi > 0 \end{cases}. \quad (18)$$

The transmission peaks frequencies are easily measurable at the output of the device. Two transmission peak degeneracy points (TPDs) arise for:

$$\epsilon = \epsilon_{TPD1} = -\Delta + \sqrt{\kappa_0^2 + \gamma_t^2} \quad (19a)$$

$$\epsilon = \epsilon_{TPD2} = -\Delta - \sqrt{\kappa_0^2 + \gamma_t^2} \quad (19b)$$

and the peak frequencies can be written as:

$$\omega_{p_{a(b)}} = \begin{cases} \omega_0 & \text{for } \xi < 0 \\ \omega_0 \pm \sqrt{(\epsilon - \epsilon_{TPD1})(\epsilon - \epsilon_{TPD2})} & \text{for } \xi > 0 \end{cases}. \quad (20)$$

In this case, it is evident that the peak frequencies show a square root dependence in the proximity of $\epsilon = \epsilon_{TPD1(2)}$. This condition corresponds to the degeneracy of the transmission peaks. There are two interesting conditions for the design of the device:
1) $\epsilon_{EP} = 0$
2) $\epsilon_{TPD1(2)} = 0$

The case with $\epsilon_{EP} = 0$ with $\Delta^2 = \kappa^2$, has been usually considered [20], [22] for the design of EP-based anti-PT-symmetric gyroscopes. However, to guarantee the maximum sensitivity of the gyroscope in the proximity of zero angular velocity, we set $\epsilon_{TPD1} = 0$. This means that our design condition becomes:

$$\Delta^2 = \kappa_0^2 + \gamma_t^2. \quad (21)$$

From an experimental point of view, the tuneability of the parameter γ_t is enough to ensure the possibility of achieving the TPD for $\epsilon_{TPD1(2)} = 0$.

C. Signal Enhancement

In order to evaluate the performance of a TPD, we define the signal scale factor as [32]:

$$SSF_{TPD}(\epsilon) = \left| \frac{1}{2}\frac{d(\Delta\omega_p)}{d\epsilon} \right|^2 \quad (22)$$

with

$$\Delta\omega_p = \begin{cases} 0 & \text{for } \xi < 0 \\ 2\sqrt{(\epsilon + \Delta)^2 - \kappa_0^2 - \gamma_t^2} & \text{for } \xi > 0 \end{cases}. \quad (23)$$

The SSF_{TPD} is equal to:

$$SSF_{TPD}(\epsilon) = \begin{cases} 0 & \text{for } \xi < 0 \\ \frac{(\epsilon + \Delta)^2}{(\epsilon + \Delta)^2 - \kappa_0^2 - \gamma_t^2} & \text{for } \xi > 0 \end{cases}. \quad (24)$$

The SSF_{TPD} diverges at $\epsilon = \epsilon_{TPD1(2)}$. In the same way, we can define a scale factor evaluating the eigenfrequency splitting as signal:

$$SSF_{EP}(\epsilon) = \left| \frac{1}{2}\frac{d(\Delta\omega_{eig})}{d\epsilon} \right|^2 \quad (25)$$

with:

$$\Delta\omega_{eig} = 2\sqrt{(\epsilon + \Delta)^2 - \kappa_0^2}. \quad (26)$$

It results:

$$SSF_{EP}\,(\epsilon) = \frac{(\epsilon + \Delta)^2}{\left|(\epsilon + \Delta)^2 - \kappa_0^2\right|}\,. \tag{27}$$

Clearly, the SSF_{EP} diverges at the EP.

D. Amplitude Noise

The properties of the non-Hermitian Hamiltonian, in the presence of noise, can be analyzed by considering the amplitude noise sources in the coupled mode theory [33] with a semiclassical approach. In particular, we will consider the five different input noises shown in (5): three of them (n_{i1}, n_{i2} and n_{ic}) arise from the coupling with external physical buses, whereas two of them ($n_{\gamma 1}$ and $n_{\gamma 2}$) arise from the coupling of the system with the gain/loss reservoirs. By using (2), (3) (with $\boldsymbol{H}$ instead of $\boldsymbol{H_0}$) and (14) we obtain in the harmonic regime:

$$\boldsymbol{y} = \left(\boldsymbol{C} + j\boldsymbol{KGK}^T\right)\boldsymbol{x}\,. \tag{28}$$

Using (5) and (28) with $s_{in} = 0$ and evaluating the output signal noise at the output of the second bus, $n_o = y_2$, we obtain:

$$n_o = j\sqrt{2\gamma_e}\sqrt{2\gamma_e}G_{21}n_{i1} + j\sqrt{2\gamma_e}\sqrt{2\gamma_e}\left(G_{21} + G_{22}\right)n_{ic}$$
$$+ \left(-1 + j\sqrt{2\gamma_e}\sqrt{2\gamma_e}G_{22}\right)n_{i2} + j\sqrt{2\gamma_e}\sqrt{2\gamma_o}G_{21}n_{\gamma 1}$$
$$+ j\sqrt{2\gamma_e}\sqrt{2\gamma_o}G_{22}n_{\gamma 2}. \tag{29}$$

Recalling that the properties of the noise sources are described by their correlations [32], here we calculate the output noise spectral density due to amplitude noise, with the same approach used in [32]. By knowing that independent sources of noise are uncorrelated, and assuming the same input noise spectral density for the three physical buses (S_i^n) and the same input noise spectral density for the two gain/loss reservoir contributions (S_γ^n), we can express the output noise spectral density (S_o^n) as:

$$S_o^n = AS_i^n + BS_\gamma^n \tag{30}$$

with

$$A = 1 + 4\gamma_e Im\,(G_{22}) + 4\gamma_e^2\left(|G_{22}|^2 + |G_{21}|^2\right)$$
$$+ 4\gamma_e^2|G_{21} + G_{22}|^2 \tag{31a}$$

$$B = 4\gamma_e\gamma_o\left(|G_{21}|^2 + |G_{22}|^2\right). \tag{31b}$$

III. FREQUENCY UNCERTAINTIES

A. Uncertainties Due to Amplitude Noise

In order to evaluate the uncertainty on the peak frequency splitting detection due to the amplitude noise modelled in the previous paragraph, we have used the same approach as in [32]. The readout of the sensor is based on the measurement of the transmission spectrum and on the measurement of the difference between the frequencies of the transmission peaks. The frequency uncertainty on the measurement of each transmission peak frequency is proportional to the linewidth (Γ) of the transmission peaks [32]. The proportionality term between the frequency uncertainty and the linewidth depends on several

parameters of acquisition and on the noise-to-signal ratio. We have assumed, as in [32], that the proportionality factor between the squared frequency uncertainty (at the transmission peaks) and the squared linewidth is dominated by the noise-to-signal ratio, evaluated at the frequencies of the transmission peaks [32], as:

$$\left(\sigma_{\Delta\omega}^N\right)^2 \propto \Gamma^2\,(\epsilon)\left(\frac{S_o^n\,(\omega = \omega_{p_a}) + S_o^n\,(\omega = \omega_{p_b})}{|s_{in}|^2\left|S_{12}\,(\omega = \omega_{p_{a(b)}})\right|^2}\right) \tag{32}$$

where the sum of the variances of the uncorrelated peak frequencies holds. Hereinafter, the proportionality coefficient between the left and right terms of (32) will be M_S. The linewidth (Γ) has been calculated as:

$$\Gamma(\epsilon) = \begin{cases} \sqrt{\xi + \sqrt{2}\sqrt{\gamma_t^4 + \left((\Delta + \epsilon)^2 - \kappa_0^2\right)^2}}, & \text{for } \xi < 0 \\ \sqrt{\xi \pm 2\gamma_t\sqrt{\left((\Delta + \epsilon)^2 - \kappa_0^2\right)} - \sqrt{\xi}}, & \text{for } \xi > 0 \end{cases} \tag{33}$$

B. Uncertainties Due to Parameters Fluctuations

Another important source of uncertainty on the peak splitting measurement is the effect of the uncertainty of Δ, κ_0 and γ_t on the peak splitting. We can calculate their relevant fluctuations scale factors:

$$FSF^\Delta = \left|\frac{d\Delta\omega_p}{d\Delta}\right|^2 = \frac{4(\epsilon + \Delta)^2}{(\epsilon + \Delta)^2 - \kappa_0^2 - \gamma_t^2} \tag{34a}$$

$$FSF^{\kappa_0} = \left|\frac{d\Delta\omega_p}{d\kappa_0}\right|^2 = \frac{4\kappa_0^2}{(\epsilon + \Delta)^2 - \kappa_0^2 - \gamma_t^2} \tag{34b}$$

$$FSF^{\gamma_t} = \left|\frac{d\Delta\omega_p}{d\gamma_t}\right|^2 = \frac{4\gamma_t^2}{(\epsilon + \Delta)^2 - \kappa_0^2 - \gamma_t^2}. \tag{34c}$$

So, the uncertainty of the output splitting due to the fluctuations on the l-th (with $l = \Delta, \kappa_0, \gamma_t$) parameter will be:

$$\left(\sigma_{\Delta\omega}^l\right)^2 = FSF^l(\sigma_l)^2. \tag{35}$$

So, the total uncertainty will be given by:

$$\left(\sigma_{\Delta\omega}^T\right)^2 = \left(\sigma_{\Delta\omega}^N\right)^2 + \left(\sigma_{\Delta\omega}^\Delta\right)^2 + \left(\sigma_{\Delta\omega}^{\kappa_0}\right)^2 + \left(\sigma_{\Delta\omega}^{\gamma_t}\right)^2. \tag{36}$$

Considering for simplicity a design with $\kappa_0 \gg \gamma_t$, we can assume $(\sigma_{\Delta\omega}^{\kappa_0})^2 \gg (\sigma_{\Delta\omega}^{\gamma_t})^2$, so that:

$$\left(\sigma_{\Delta\omega}^T\right)^2 \approx \left(\sigma_{\Delta\omega}^N\right)^2 + \left(\sigma_{\Delta\omega}^\Delta\right)^2 + \left(\sigma_{\Delta\omega}^{\kappa_0}\right)^2 = \left(\sigma_{\Delta\omega}^N\right)^2 + \left(\sigma_{\Delta\omega}^F\right)^2 \tag{37}$$

where $\sigma_{\Delta\omega}^F$ represents the fraction of uncertainty related to the fluctuations of κ_0 and Δ.

C. Comparison With a Classical Resonant Sensor

In order to evaluate the performance of the TPD-based sensor, we consider a new device with the same effective Hamiltonian, but with null coupling strength, thus making the two resonators uncoupled. This can be physically imagined as separating the two resonators, duplicating the intermediate bus and reading
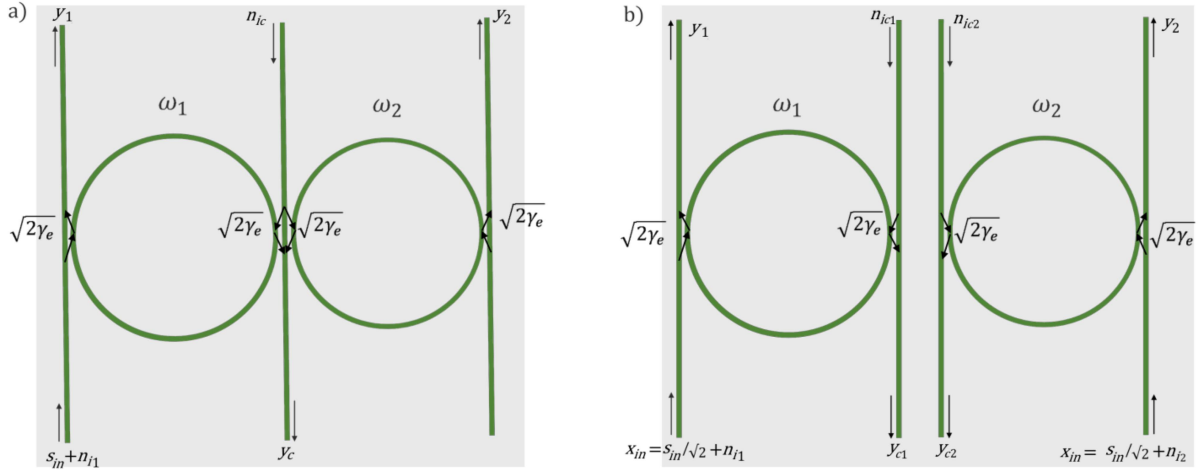
Fig. 2.   Schematic of the anti-PT-symmetric gyroscope (a) and of the uncoupled architecture with two resonators (b), with labels of input signals and noises, and output signals.

the output at the drop port of each resonator (see Fig. 2). The uncoupled effective Hamiltonian becomes:

$$\boldsymbol{H}_u = \begin{pmatrix} \omega_0 + \Delta + j\gamma_t + \epsilon & 0 \\ 0 & \omega_0 - \Delta + j\gamma_t - \epsilon \end{pmatrix}. \tag{38}$$

In this case the two resonators can be studied separately, leading to two different peak frequencies (equal to the real part of the eigenfrequencies, in this case):

$$\omega_{u_a} = \omega_0 + \Delta + \epsilon \tag{39a}$$
$$\omega_{u_b} = \omega_0 - \Delta - \epsilon \tag{39b}$$

with linewidth:

$$\Gamma_u = \gamma_t \tag{40}$$

and the elements of the Green's matrix:

$$G_{u11} = \frac{1}{\omega_0 + \Delta + j\gamma_t + \epsilon - \omega} \tag{41a}$$
$$G_{u12} = G_{u21} = 0 \tag{41b}$$
$$G_{u22} = \frac{1}{\omega_0 - \Delta + j\gamma_t - \epsilon - \omega}. \tag{41c}$$

The input-output transmission at the drop ports of each resonator is found as (with x_{in} the input signal and $y_{c1(2)}$ the output signal at the drop port):

$$T_{1d,u} = |y_{c1}/x_{in}|^2 = 4\gamma_e^2|G_{u11}|^2 \tag{42a}$$
$$T_{2d,u} = |y_{c2}/x_{in}|^2 = 4\gamma_e^2|G_{u22}|^2. \tag{42b}$$

We can then define a signal scale factor for the uncoupled Hamiltonian:

$$SSF_u = \left| \frac{1}{2} \frac{d(\Delta\omega_u)}{d\epsilon} \right|^2 = 1 \tag{43}$$

with $\Delta\omega_u = \omega_{ua} - \omega_{ub}$. The noise amplitudes at the drop port of each resonator become:

$$n_{u1} = j\sqrt{2\gamma_e}\sqrt{2\gamma_e}G_{u11}n_{i1}$$
$$+ \left(-1 + j\sqrt{2\gamma_e}\sqrt{2\gamma_e}G_{u11}\right)n_{ic1}$$

$$+ j\sqrt{2\gamma_e}\sqrt{2\gamma_o}G_{u11}n_{\gamma 1} \tag{44a}$$

$$n_{u2} = j\sqrt{2\gamma_e}\sqrt{2\gamma_e}G_{u22}n_{i2}$$
$$+ \left(-1 + j\sqrt{2\gamma_e}\sqrt{2\gamma_e}G_{u22}\right)n_{ic2}$$
$$+ j\sqrt{2\gamma_e}\sqrt{2\gamma_o}G_{u22}n_{\gamma 2} \tag{44b}$$

and the noise spectral density:

$$S_{o,u_1}^n = A_{u1} S_i^n + B_{u1} S_\gamma^n \tag{45a}$$
$$S_{o,u_2}^n = A_{u2} S_i^n + B_{u2} S_\gamma^n \tag{45b}$$

with

$$A_{u1} = 4\gamma_e^2|G_{u11}|^2 + |-1 + j2\gamma_e G_{u11}|^2 \tag{46a}$$
$$B_{u1} = 4\gamma_e\gamma_o|G_{u11}|^2 \tag{46b}$$
$$A_{u2} = 4\gamma_e^2|G_{u11}|^2 + |-1 + j2\gamma_e G_{u22}|^2 \tag{46c}$$
$$B_{u2} = 4\gamma_e\gamma_o|G_{u22}|^2. \tag{46d}$$

Considering the two uncoupled rings, each of them is supplied with half of the power $(0.5|s_{in}|^2)$ of the anti-PT-symmetric version (see Fig. 2) for comparison reason (same total input power as in the anti-PT-symmetric version).

The squared uncertainty on the difference between ω_{ua} and ω_{ub} is:

$$\left(\sigma_{\Delta\omega,u}^N\right)^2 \propto \Gamma_u^2(\epsilon) \frac{S_{o,u_1}^n(\omega = \omega_{u_a}) + S_{o,u_2}^n(\omega = \omega_{u_b})}{\frac{1}{2}|s_{in}|^2|S_{1d,u}|^2(\omega = \omega_{u_{a(b)}})}. \tag{47}$$

The proportionality coefficient between the left and right terms is M_S.

Now we also include the effect of fluctuations of design parameters. In this case the only effect is due to the fluctuations of Δ. We define the fluctuations scale factor in the uncoupled system (FSF_u):

$$FSF_u = \left| \frac{d\Delta\omega_u}{d\Delta} \right|^2 = 4 \tag{48}$$

TABLE I
PARAMETERS USED IN SIMULATIONS

Symbol	Value
c	$3 \cdot 10^8$ m/s
λ_0	$1.55\ \mu$m
ω_0	$2\pi c/\lambda_0$
γ_0	$2\kappa_0 - \gamma_t \approx 3.78 \cdot 10^{-6} \cdot \omega_0$
γ_e	$\kappa_0 \approx 1.99 \cdot 10^{-6} \cdot \omega_0$
γ_t	$2 \cdot 10^{-7} \cdot \omega_0$
Δ	$2 \cdot 10^{-6} \cdot \omega_0$
κ_0	$(\Delta^2 - \gamma_t^2)^{1/2} \approx 1.99 \cdot 10^{-6} \cdot \omega_0$

The uncertainty on the output splitting in the uncoupled case is:

$$\left(\sigma_{\Delta\omega,u}^{\Delta}\right)^2 = FSF_u(\sigma_\Delta)^2. \tag{49}$$

Finally, the total uncertainty in the uncoupled sensor is:

$$\left(\sigma_{\Delta\omega,u}^T\right)^2 = \left(\sigma_{\Delta\omega,u}^N\right)^2 + \left(\sigma_{\Delta\omega,u}^{\Delta}\right)^2. \tag{50}$$

Eventually we define two metrics to compare the TPD-based sensor and the sensor realized with uncoupled resonator:

$$\chi_{\Delta\omega} = \frac{SSF_{TPD}}{SSF_u} \tag{51a}$$

$$\chi_\sigma = \frac{\left(\sigma_{\Delta\omega}^T\right)^2}{\left(\sigma_{\Delta\omega,u}^T\right)^2}. \tag{51b}$$

In particular $\chi_{\Delta\omega}$ (χ_σ) represents the enhancement of the frequency peak splitting (uncertainties) of a TPD-based sensor with respect to the uncoupled case. If the ratio between them, $\chi_{\Delta\omega}/\chi_\sigma$, is higher than 1, it means that setting up a non-Hermitian system for sensing shows a better signal-to-noise ratio than a classical (uncoupled) sensor. Hereinafter, we will refer to the uncoupled version as the "classical" sensor.

IV. NUMERICAL SIMULATIONS

In this section the results of some numerical simulations are shown. In particular, we will consider, without losing any generality, the parameters in Table I.

The color plot in Fig. 3 shows the transmission T_{12} as a function of the normalized frequency difference $(\omega-\omega_0)/\omega_0$ and of the perturbation ϵ applied to the resonators, due to rotation. It is evident that for $\epsilon > \epsilon_{TPD} = 0$ the frequency peaks (red dashed lines) diverge as the square root of the perturbation. In the same graph also the eigenfrequencies are shown (black dash-dotted lines). As expected, they diverge between each other according to a square root dependence around $\epsilon = \epsilon_{EP}$.

Fig. 4 shows the signal scale factor of the peak frequency splitting (SSF_{TPD}) and the signal scale factor of the eigenfrequencies (SSF_{EP}). As expected, the signal scale factor related to the eigenfrequencies diverges at the exceptional point. And it is evident that the SSF_{TPD} diverges at a different value of the perturbation (ϵ_{TPD}), so explaining the advantage of using the frequency splitting between transmission peaks as the output of the sensor.
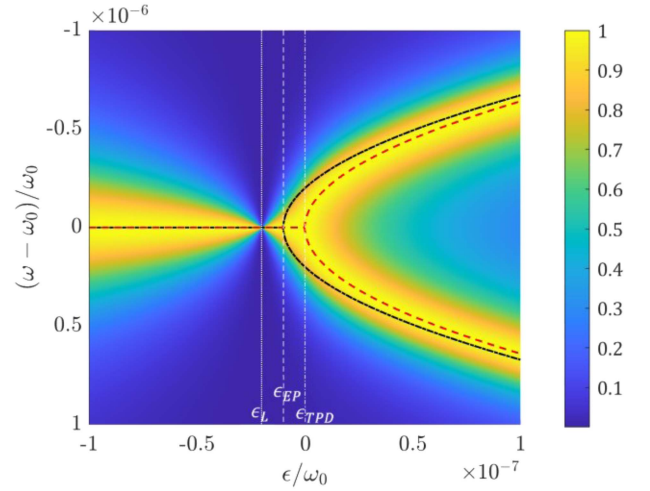

Fig. 3. Transmission $T_{12} = |y_2/s_{in}|^2$ as a function of normalized frequency detuning from ω_0 and of the normalized perturbation (ϵ/ω_0).
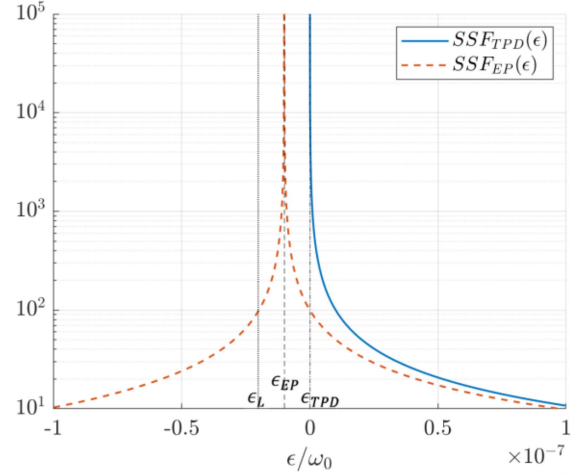

Fig. 4. SSF_{TPD} and SSF_{EP} as a function of the normalized perturbation.

Fig. 5 shows the output noise spectral density, divided by the sum of the power spectral density at the input bus and at the gain/loss reservoir ($S_i^n + S_\gamma^n$), for two values of S_γ^n/S_i^n. It can be noted that the output noise at the transmission peak frequencies diverges at the lasing frequency. The curves in Fig. 5 for different ratios S_γ^n/S_i^n result to be superposed, because of the simulation hypothesis $\kappa_0 >> \gamma_t$.

The bi-logarithmic graph in Fig. 6 shows the different uncertainties on the peak frequency splitting in the non-Hermitian gyroscope (solid lines) and in the classical one (dashed lines), as a function of the perturbation in the proximity of the TPD ($\epsilon \to \epsilon_{TPD}$). All the uncertainties are normalized to the central frequency ω_0 and the ones due to amplitude noise ($\sigma_{\Delta\omega}^N$ and $\sigma_{\Delta\omega,u}^N$) are further normalized to $M_S^{1/2}$. In particular, the uncertainties on the peak frequency splitting due to parameters fluctuations ($\sigma_{\Delta\omega}^F$ and $\sigma_{\Delta\omega,u}^F$) are shown with blue, red and yellow curves. Instead, the uncertainties on the peak frequency splitting due to amplitude noise ($\sigma_{\Delta\omega}^N$ and $\sigma_{\Delta\omega,u}^N$) are shown with
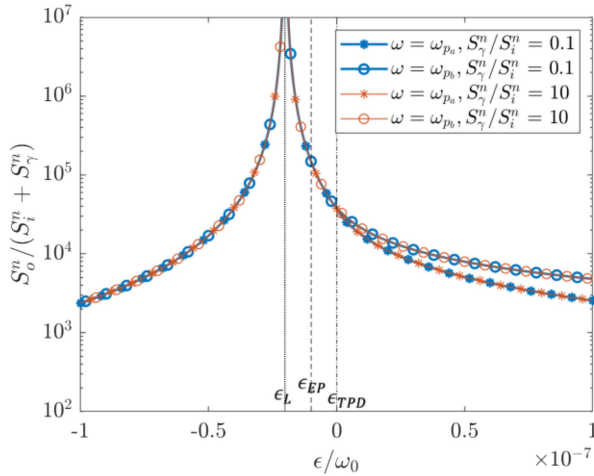
Fig. 5. Output noise spectral density at the transmission peak frequencies with a semiclassical approach divided by the sum of the power spectral density at the input bus and at the gain/loss reservoir ($S_i^n + S_\gamma^n$), for two values of the ratio S_γ^n/S_i^n.
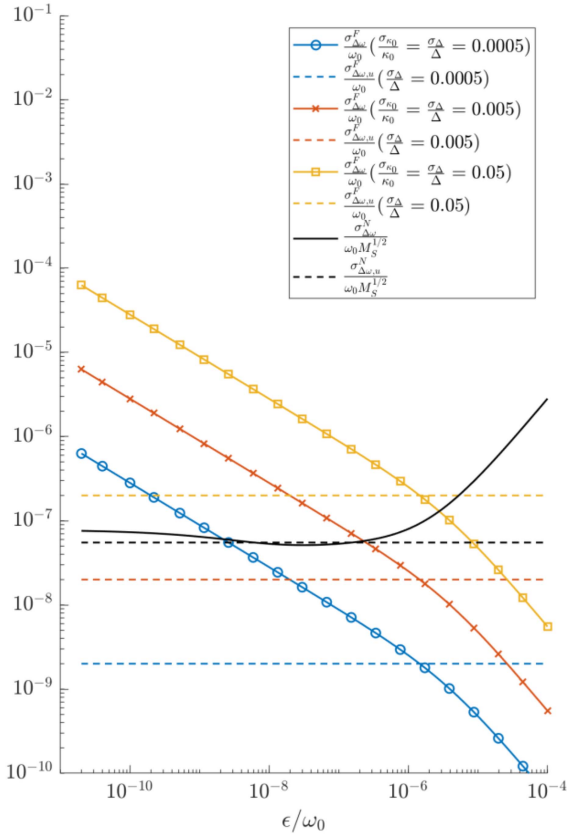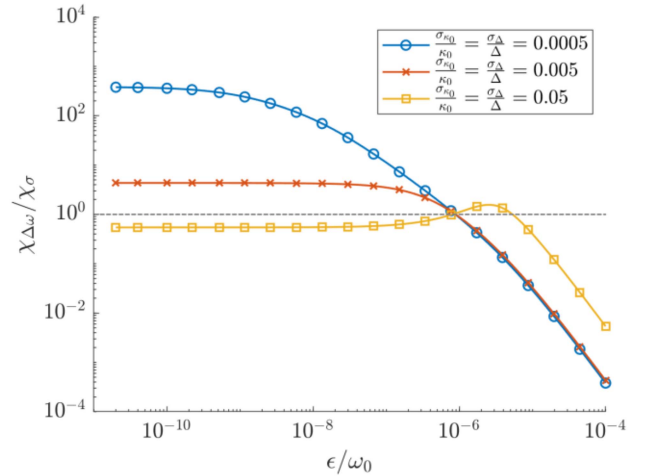

Fig. 7. Ratio between $\chi_{\Delta\omega}$ and χ_σ for different values of uncertainties due to fluctuations of parameters, for a ratio S_γ^n/S_i^n equal to 10 and $|s_{in}|^2/(S_i^n + S_\gamma^n)$ equal to 20 dB. Above unity (dashed line) the NH sensor has a better signal-to-noise ratio than a classical sensor. The simulations are performed for $M_S = 1$. To estimate the linear dependence of $\chi_{\Delta\omega}/\chi_\sigma$ from M_S, for $\epsilon \rightarrow \epsilon_{\text{TPD}}$, (51) and (46) can be used.

Fig. 6. Different sources of uncertainties in the non-Hermitian gyroscope (solid lines) and in the classical one (dashed lines), as a function of the perturbation in the proximity of the TPD ($\epsilon = \epsilon_{\text{TPD}}$), for a fixed ratio S_γ^n/S_i^n equal to 10 and $|s_{in}|^2/(S_i^n + S_\gamma^n)$ equal to 20 dB.

black curves. The simulations related to the uncertainties on the peak frequency splitting due to parameters fluctuations ($\sigma_{\Delta\omega}^F$ and $\sigma_{\Delta\omega,u}^F$) have been performed for different values of the relative uncertainties of the design parameters ($\sigma_{\kappa_0}/\kappa_0$ and σ_Δ/Δ, that for simplicity have been considered to be the same). The chosen

values for these relative uncertainties of the design parameters ($\sigma_{\kappa_0}/\kappa_0$ and σ_Δ/Δ) have been chosen according to literature: the measurements in [34] suggest a worst-case approximation of the relative uncertainty of the coupling strength of an InP-based coupler lower than 1%, while the measurements in [35] suggest a worst-case approximation for the relative uncertainty of the resonance of a silicon resonator (proportional to the relative uncertainty of resonance half difference Δ) of 005%. Thus, we can conclude that the analyzed range of relative uncertainties of parameters (from 0.05% to 5%) in Fig. 6 can be representative of experimental data of resonators in different mature technologies. In order to compare the effects of the uncertainty on the peak frequency splitting due to amplitude noise and the one due to parameters fluctuations, the ratio S_γ^n/S_i^n is set to 10 and $|s_{in}|^2/(S_i^n + S_\gamma^n)$ is set to 20 dB in all the simulations.

From Fig. 6 it can be seen that for $\epsilon \gg \kappa_0$ the uncertainty on the peak frequency splitting due to amplitude noise in the NH case ($\sigma_{\Delta\omega}^N$) increases for increasing values of ϵ. Intuitively, this trend depends on the fact that for $\epsilon \gg \kappa_0$ the transfer function T_{12} (equal to $|y_2/s_{in}|^2$) reduces as the perturbation increases (see (16) and (32)).

It is worth noting that by considering y_1 as the output in both the configurations (see Fig. 2(a) and (b)), the transfer function and the uncertainties on the peak frequency splitting tends to be equal for the NH and the uncoupled configurations when $\epsilon \gg \kappa_0$, thus confirming the validity of the model.

Finally, Fig. 7 shows the ratio between $\chi_{\Delta\omega}$ and χ_σ, assuming $S_\gamma^n/S_i^n = 10$ and $|s_{in}|^2/(S_i^n + S_\gamma^n) = 20$ dB. The ratio $\chi_{\Delta\omega}/\chi_\sigma$ is a useful way to compare the performance of a NH anti-PT-symmetric gyroscope with classical resonant gyroscopes. A ratio higher than unity demonstrates the clear advantage of the use of a NH gyroscope with respect to a classical one. In simulations, different values of the relative uncertainty on the parameter Δ have been considered for the classical ring resonator gyroscope.

The same value of relative uncertainty has been considered for both the parameter Δ and κ_0 in the anti-PT-symmetric case. The value of the uncertainties used for the simulations in Fig. 7 corresponds to those analyzed in Fig. 6.

The simulations show that when the uncertainties related to the fluctuations of the design parameter Δ (and κ_0) are lower than the uncertainty due to the amplitude noise in the classical configuration ($\sigma_{\kappa 0}, \sigma_\Delta << \sigma_{\Delta\omega,u}^N$, blue and red curves in Fig. 6), an anti-PT-symmetric system operating close to TPD can perform better than the classical sensor (uncoupled version) in terms of signal-to-noise ratio.

It is possible to notice that for $\epsilon \to \epsilon_{\text{TPD}}$, the ratio $\chi_{\Delta\omega}/\chi_\sigma$ tends to a constant value. In particular, since for $\epsilon \to \epsilon_{\text{TPD}}$, the uncertainty due to fluctuations is much higher (diverges at TPD) than the uncertainty due to amplitude noise ($\sigma_{\Delta\omega}^F >> \sigma_{\Delta\omega}^N$ close to TPD), the ratio $\chi_{\Delta\omega}/\chi_\sigma$ can be approximated as:

$$\frac{\chi_{\Delta\omega}}{\chi_\sigma} \approx \frac{(\epsilon_{TPD}+\Delta)^2}{4(\epsilon_{TPD}+\Delta)^2\sigma_\Delta^2 + 4\kappa_0^2\sigma_{\kappa_0}^2}\left[\left(\sigma_{\Delta\omega,u}^N\right)^2 + \left(\sigma_{\Delta\omega,u}^\Delta\right)^2\right].$$
$$(52)$$

From Fig. 7, it can be noted that as the perturbation ϵ tends to infinity, the anti-PT-symmetric sensor performs much worse than the classical sensor (uncoupled version) and the figure of merit $\chi_{\Delta\omega}/\chi_\sigma$ tends to zero. This is due to the divergence of the uncertainty $\sigma_{\Delta\omega}^N$ for increasing values of ϵ (with $\epsilon >> \kappa_0$) (see Fig. 6). However, we would like to underline that the possible improvement of the anti-PT-symmetric gyroscope with respect to the classical sensor is seen at small values of the perturbation ($\epsilon \to \epsilon_{TPD}$), that represents the interesting region for most sensing applications.

The result in Fig. 7 shows that non-Hermitian Hamiltonians can effectively improve the sensing performance in the proximity of the EPs, more specifically close to the TPDs. In this context, the concept of exceptional surface (ES) has been already proposed to strongly reduce the influence of the fluctuations of parameters [36], thus representing a robust alternative to increase the signal-to-noise ratio of non-Hermitian sensing.

V. CONCLUSION

In this article we have analyzed an anti-PT-symmetric gyroscope and compared its signal-to-noise performance with a classical resonant gyroscope. Rather than using the eigenfrequency splitting as the measurable output, we consider the frequency splitting of the transmission peaks, which coalesce at the so-called transmission peak degeneracy.

We have analyzed two different sources of uncertainty both for the non-Hermitian and for the classical case: amplitude noise arising from input ports and gain/loss reservoirs and fluctuations in the design parameters.

We have then considered two new figures of merit defined as the ratio between the enhancement in the signal (signal scale factor) between a non-Hermitian gyroscope and a classical one and the enhancement in the uncertainties between a non-Hermitian gyroscope and a classical one. The ratio between them is useful to understand the real advantage of using a non-Hermitian sensor with respect to a classical one. We have demonstrated that when in the classical sensor the uncertainty due to fluctuations

is negligible with respect to the uncertainty due to amplitude noise, the non-Hermitian sensor can perform better in terms of signal-to-noise ratio near to the transmission peak degeneracy. Whereas, when in the classical gyroscope, the uncertainty due to fluctuations is dominant with respect to the one due to amplitude noise, the non-Hermitian sensor shows worse signal-to-noise ratio than a classical gyroscope.

We would like to underline that the aim of the manuscript is not to demonstrate the absolute supremacy of non-Hermitian sensing with respect to the classical sensing in terms of signal-to-noise ratio. Indeed, our approach provides a guideline related to the operating conditions (related to fluctuations uncertainty and amplitude noise) for which setting up a non-Hermitian sensor could benefit from an increased signal-to-noise ratio with respect to the classical sensor.

REFERENCES

[1] M-A. Miri and A. Alù, "Exceptional points in optics and photonics," *Science*, vol. 363, no. 6422, Jan. 2019, Art. no. eaar7709, doi: 10.1126/science.aar7709.

[2] J. Wiersig, "Review of exceptional point-based sensors," *Photon. Res.*, vol. 8, no. 9, pp. 1457–1467, Aug. 2020, doi: 10.1364/prj.396115.

[3] C. M. Bender and S. Boettcher, "Real spectra in non-Hermitian hamiltonians having PT symmetry," *Phys. Rev. Lett.*, vol. 80, no. 24, pp. 5243–5246, Jun. 1998, doi: 10.1103/physrevlett.80.5243.

[4] B. Peng et al., "Parity–Time-symmetric whispering-gallery microcavities," *Nature Phys.*, vol. 10, no. 5, pp. 394–398, Apr. 2014, doi: 10.1038/nphys2927.

[5] H. Hodaei et al., "Enhanced sensitivity at higher-order exceptional points," *Nature*, vol. 548, no. 7666, pp. 187–191, Aug. 2017, doi: 10.1038/nature23280.

[6] H. Zhao, Z. Chen, R. Zhao, and L. Feng, "Exceptional point engineered glass slide for microscopic thermal mapping," *Nature Commun.*, vol. 9, no. 1, May 2018, Art. no. 1764, doi: 10.1038/s41467-018-04251-3.

[7] P. Djorwe, Y. Pennec, and B. Djafari-Rouhani, "Exceptional point enhances sensitivity of optomechanical mass sensors," *Phys. Rev. Appl.*, vol. 12, no. 2, Aug. 2019, Art. no. 024002, doi: 10.1103/physrevapplied.12.024002.

[8] Y. Cao and P. Yan, "Exceptional magnetic sensitivity PT-symmetric cavity magnon polaritons," *Phys. Rev. B*, vol. 99, no. 21, Jun. 2019, Art. no. 214415, doi: 10.1103/physrevb.99.214415.

[9] J.-H. Park et al., "Symmetry-breaking-induced plasmonic exceptional points and nanoscale sensing," *Nature Phys.*, vol. 16, no. 4, pp. 462–468, Feb. 2020, doi: 10.1038/s41567-020-0796-x.

[10] T. Xing et al., "Ultrahigh sensitivity stress sensing method near the exceptional point of parity-time symmetric systems," *J. Phys. D: Appl. Phys.*, vol. 53, no. 20, Mar. 2020, Art. no. 205102, doi: 10.1088/1361-6463/ab761d.

[11] Y. Liu, P. Yan, F. Liu, A. Jian, and S. Sang, "Biosensing near the exceptional point based on resonant optical tunneling effect," *Micromachines*, vol. 12, no. 4, p. 426, Apr. 2021, doi: 10.3390/mi12040426.

[12] P. Nie et al., "Gas sensing near exceptional points," *J. Phys. D: Appl. Phys.*, vol. 54, no. 25, Apr. 2021, Art. no. 254001, doi: 10.1088/1361-6463/abf167.

[13] X. Liu, H. Wang, J. Zhang, J. Guo, and X. Wu, "Enhancement of sensitivity near exceptional point by constructing nonreciprocal fiber cavity assisted by isolator and erbium-doped fiber," *IEEE Sensors J.*, vol. 21, no. 17, pp. 18823–18828, Sep. 2021, doi: 10.1109/jsen.2021.3092058.

[14] P.-Y. Chen et al., "Generalized parity–Time symmetry condition for enhanced sensor telemetry," *Nature Electron.*, vol. 1, no. 5, pp. 297–304, May 2018, doi: 10.1038/s41928-018-0072-6.

[15] Y. Choi, C. Hahn, J. W. Yoon, and S. H. Song, "Observation of an anti-PT-symmetric exceptional point and energy-difference conserving dynamics in electrical circuit resonators," *Nature Commun.*, vol. 9, no. 1, Jun. 2018, Art. no. 2182, doi: 10.1038/s41467-018-04690-y.

[16] Z. Dong, Z. Li, F. Yang, C.-W. Qiu, and J. S. Ho, "Sensitive readout of implantable microsensors using a wireless system locked to an exceptional point," *Nature Electron.*, vol. 2, no. 8, pp. 335–342, Aug. 2019, doi: 10.1038/s41928-019-0284-4.

[17] J. Ren et al., "Ultrasensitive micro-scale parity-time-symmetric ring laser gyroscope," *Opt. Lett.*, vol. 42, no. 8, Art. no. 1556, Apr. 2017, doi: 10.1364/ol.42.001556.

[18] M. De Carlo, F. De Leonardis, and V. M. N. Passaro, "Design rules of a microscale PT-Symmetric optical gyroscope using group IV platform," *J. Lightw. Technol.*, vol. 36, no. 16, pp. 3261–3268, Aug. 2018, doi: 10.1109/jlt.2018.2837754.

[19] M. P. Hokmabadi, A. Schumer, D. N. Christodoulides, and M. Khajavikhan, "Non-Hermitian ring laser gyroscopes with enhanced Sagnac sensitivity," *Nature*, vol. 576, no. 7785, pp. 70–74, Dec. 2019, doi: 10.1038/s41586-019-1780-4.

[20] M. De Carlo, F. De Leonardis, L. Lamberti, and V. M. N. Passaro, "High-sensitivity real-splitting anti-PT-symmetric microscale optical gyroscope," *Opt. Lett.*, vol. 44, no. 16, Aug. 2019, Art. no. 3956, doi: 10.1364/ol.44.003956.

[21] Y-H. Lai, Y-K. Lu, M-G. Suh, Z. Yuan, and K. Vahala, "Observation of the exceptional-point-enhanced Sagnac effect," *Nature*, vol. 576, no. 7785, pp. 65–69, Dec. 2019, doi: 10.1038/s41586-019-1777-z.

[22] M. De Carlo, F. De Leonardis, L. Lamberti, and V. M. N. Passaro, "Design of a resonator-bus-resonator anti-parity-time-symmetric integrated optical gyroscope," *Opt. Lasers Eng.*, vol. 153, Jun. 2022, Art. no. 106983, doi: 10.1016/j.optlaseng.2022.106983.

[23] J. Wiersig, "Enhancing the sensitivity of frequency and energy splitting detection by using exceptional points: Application to microcavity sensors for single-particle detection," *Phys. Rev. Lett.*, vol. 112, no. 20, May 2014, Art. no. 203901, doi: 10.1103/physrevlett.112.203901.

[24] W. Chen, Ş. Kaya Özdemir, G. Zhao, J. Wiersig, and L. Yang, "Exceptional points enhance sensing in an optical microcavity," *Nature*, vol. 548, no. 7666, pp. 192–196, Aug. 2017, doi: 10.1038/nature23281.

[25] W. Li et al., "Real frequency splitting indirectly coupled anti-parity-time symmetric nanoparticle sensor," *J. Appl. Phys.*, vol. 128, no. 13, Oct. 2020, Art. no. 134503, doi: 10.1063/5.0020944.

[26] H. Zhang et al., "Breaking anti-PT symmetry by spinning a resonator," *Nano Lett.*, vol. 20, no. 10, pp. 7594–7599, Sep. 2020, doi: 10.1021/acs.nanolett.0c03119.

[27] W. Chen, J. Zhang, B. Peng, Ş. K. Özdemir, X. Fan, and L. Yang, "Parity-time-symmetric whispering-gallery mode nanoparticle sensor," *Photon. Res.*, vol. 6, no. 5, pp. A23–A30, Apr. 2018, doi: 10.1364/prj.6.000a23.

[28] H. K. Lau and A. A. Clerk, "Fundamental limits and non-reciprocal approaches in non-Hermitian quantum sensing," *Nature Commun.*, vol. 9, no. 1, Oct. 2018, Art. no. 4320, doi: 10.1038/s41467-018-06477-7.

[29] H. Wang, Y.-H. Lai, Z. Yuan, M.-G. Suh, and K. Vahala, "Petermann-factor sensitivity limit near an exceptional point in a Brillouin ring laser gyroscope," *Nature Commun.*, vol. 11, no. 1, Mar. 2020, Art. no. 1610, doi: 10.1038/s41467-020-15341-6.

[30] J. Wiersig, "Prospects and fundamental limits in exceptional point-based sensing," *Nature Commun.*, vol. 11, no. 1, May 2020, Art. no. 2454, doi: 10.1038/s41467-020-16373-8.

[31] D. D. Smith, H. Chang, E. Mikhailov, and S. M. Shahriar, "Beyond the Petermann limit: Prospect of increasing sensor precision near exceptional points," *Phys. Rev. A*, vol. 106, no. 1, Jul. 2022, Art. no. 013520, doi: 10.1103/physreva.106.013520.

[32] R. Kononchuk, J. Cai, F. Ellis, R. Thevamaran, and T. Kottos, "Exceptional-point-based accelerometers with enhanced signal-to-noise ratio," *Nature*, vol. 607, no. 7920, pp. 697–702, Jul. 2022, doi: 10.1038/s41586-022-04904-w.

[33] W. Suh, Z. Wang, and S. Fan, "Temporal coupled-mode theory and the presence of non-orthogonal modes in lossless multimode cavities," *IEEE J. Quantum Electron.*, vol. 40, no. 10, pp. 1511–1518, Oct. 2004, doi: 10.1109/jqe.2004.834773.

[34] A. E. Kaplan, G. Bellanca, J. P. van Engelen, Y. Jiao, J. J. G. M. van der Tol, and P. Bassi, "Experimental characterization of directional couplers in InP photonic membranes on silicon (IMOS)," *OSA Continuum*, vol. 2, no. 10, pp. 2844–2854, Sep. 2019, doi: 10.1364/osac.2.002844.

[35] M. S. Luchansky and R. C. Bailey, "Silicon photonic microring resonators for quantitative cytokine detection and T-cell secretion analysis," *Anal. Chem.*, vol. 82, no. 5, pp. 1975–1981, Feb. 2010, doi: 10.1021/ac902725q.

[36] Q. Zhong, J. Ren, M. Khajavikhan, D. N. Christodoulides, Ş. K. Özdemir, and R. El-Ganainy, "Sensing with exceptional surfaces in order to combine sensitivity with robustness," *Phys. Rev. Lett.*, vol. 122, no. 15, Apr. 2019, Art. no. 153902, doi: 10.1103/physrevlett.122.153902.

[37] H. Zhou, J. Y. Lee, S. Liu, and B. Zhen, "Exceptional surfaces in PT-symmetric non-Hermitian photonic systems," *Optica*, vol. 6, no. 2, pp. 190–193, Feb. 2019, doi: 10.1364/optica.6.000190.